# Defect-induced anomalous thermal quenching of photoluminescence in the transition metal dichalcogenide ternary alloy $Mo_{0.6}W_{0.4}Se_2$

Navya Biju, Prahalad Kanti Barman, Jibin N. Sunil, and Rajeev N. Kini*

*Indian Institute of Science Education and Research Thiruvananthapuram (IISER-TVM), Maruthamala P.O. Vithura, Kerala 695551, India*

(Received 24 October 2023; revised 18 April 2024; accepted 12 June 2024; published 24 June 2024)

We report negative thermal quenching of photoluminescence (PL) in few-layered $Mo_{0.6}W_{0.4}Se_2$ flakes. A comparative study of temperature-dependent PL from two groups of $Mo_{0.6}W_{0.4}Se_2$ flakes, one with defects and the other with negligible defects, shows that this anomalous enhancement in the PL with increasing temperature is due to the dissociation of defect-bound excitons at higher temperatures. The relaxation dynamics of the carriers localized at these defect states were studied using the ultrafast pump-probe technique, which shows that the photogenerated carriers are trapped at these defects on a timescale of ≈3 ps.

DOI: 10.1103/PhysRevMaterials.8.064005

## I. INTRODUCTION

In recent years, the field of materials science has witnessed a surge of interest in atomically thin two-dimensional (2D) transition metal dichalcogenides (TMDCs) owing to their interesting optoelectronic properties [1–5]. This intrigue stems from their remarkable characteristics, including the transition from an indirect to a direct band gap as the bulk material is thinned to the monolayer limit, a large exciton binding energy even at room temperature, and intriguing coupled spin-valley physics [4]. Consequently, TMDCs have emerged as promising candidates for many applications, ranging from photodetectors, photocatalysts, and flexible wearable electronics to energy storage technologies [6–9]. Notably, alloying has emerged as a potent strategy to tailor the optical and electronic properties of 2D TMDCs. By judiciously altering the ratio of transition metal atoms ($M$ and $M'$) or chalcogen atoms ($X$ and $X'$), novel alloys such as $M_xM'_{1-x}X_2$ or $MX'_yX_{2-y}$ can be synthesized, broadening the spectrum of potential applications [10–13]. However, defects, such as chalcogen vacancies, have been observed and significantly influence the material's optoelectronic properties by creating localized deep-level trap states [14,15]. Understanding the interplay between these defects and carrier dynamics is pivotal, as it profoundly impacts the carrier transport and optical behavior, ultimately affecting the performance of devices based on TMDCs and TMDC alloys.

In this paper, we delve into the role played by defects in TMDC alloys in determining the photogenerated carrier dynamics. Photoluminescence (PL) measurements show enhancement in luminescence with increasing temperature, which is termed negative thermal quenching (NTQ). We show that this NTQ of PL is due to the dissociation of the defect-bound excitons upon temperature increase, causing an enhancement in the intensity of neutral excitons. Density functional theory (DFT) calculations support the presence of defect states due to chalcogen vacancies, which are known to be prevalent in TMDCs. Transient reflectivity measurements unveil the effect of defect-related relaxation pathways on the dynamics of optically generated carriers.

## II. SAMPLES AND EXPERIMENTS

The flux zone-grown $Mo_{0.6}W_{0.4}Se_2$ crystals were procured from 2D Semiconductors Inc. The $Mo_{0.6}W_{0.4}Se_2$ flakes were mechanically exfoliated onto $SiO_2/Si$ substrates from the bulk $Mo_{0.6}W_{0.4}Se_2$ crystal. The optical microscope images, optical contrast images, and atomic force microscopy (AFM) images are shown in Supplemental Material Fig. S1 [16]. The thicknesses of the flakes were obtained using AFM measurements and further confirmed using optical contrast measurements [17]. We studied six flakes of $Mo_{0.6}W_{0.4}Se_2$ with different thicknesses ranging from monolayer to six-layered flakes, and the thickness of the flakes is indicated in Supplemental Material Fig. S1 [16]. The Raman spectra were obtained using a Raman microscope (XploRa PLUS, Horiba Scientific) with 532-nm laser excitation. The Raman spectra of the flakes are shown in Supplemental Material Fig. S3 [16]. The out-of-plane $A_{1g}$ mode is at ≈245.6 $cm^{-1}$, and the $E^1_{2g}$ mode is at ≈292.2 $cm^{-1}$ for all six flakes. By comparing the Raman modes with an exfoliated monolayer of $Mo_xW_{1-x}Se_2$, which was previously reported, we confirm the alloy to be $Mo_{0.6}W_{0.4}Se_2$, which is in agreement with the XPS data discussed later [10]. The presence of the $B^1_{2g}$ mode at 346.4 $cm^{-1}$ in the alloy samples provides further confirmation of the composition [10].

X-ray photoemission spectroscopy (XPS) measurements on the bulk crystal were carried out using an Omicron Nanotechnology XPS system, and the XPS data were analyzed by CasaXPS using Shirley background correction to estimate the composition of the $Mo_xW_{1-x}Se_2$ alloy crystal. The XPS spectra are shown in Supplemental Material Fig. S4 [16]. The spectra show (i) core level (CL) binding energy peaks of Mo $3d_{5/2}$ and $3d_{3/2}$ at 229.6 and 232.6 eV, respectively; (ii) CL peaks at 33.5 and 35.6 eV representing W $4f_{7/2}$ and $4f_{5/2}$ respectively; and (ii) CL binding energy peaks of Se $3d_{5/2}$ and $3d_{3/2}$, which are attributed to divalent selenium

*Contact author: rajeevkini@iisertvm.ac.in

 

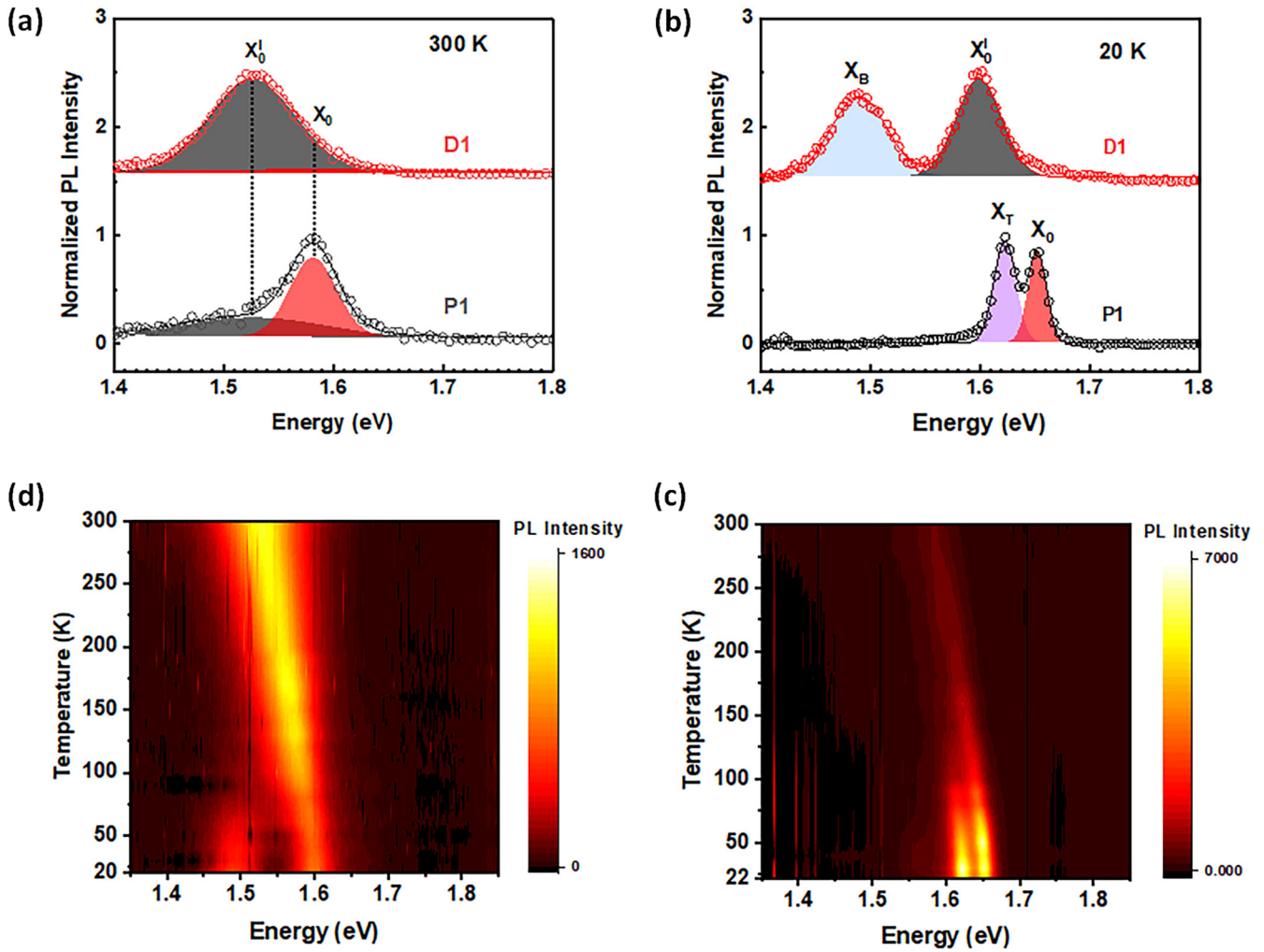


FIG. 1. The PL spectra of samples D1 and P1 at (a) 300 K and (b) 20 K. The 2D color plot of temperature-dependent PL spectra for samples (c) P1 and (d) D1.

ions, at 55.6 and 56.5 eV, respectively [18–20]. The elemental composition was extracted from the relative percentage of the total normalized area of the Mo, W, and Se peaks, yielding the composition of the alloy as $Mo_{0.6}W_{0.4}Se_2$.

Temperature-dependent PL measurements were performed using a homebuilt micro-PL setup in the backscattering configuration. A 633-nm He-Ne laser with an average laser power of 500 μW was used as the excitation source for PL measurements. The excitation light was focused on the sample using a 10× objective (NA = 0.24), which gave a spot size of ≈3 μm diameter. PL was collected with the same objective and analyzed using a 0.32-m monochromator (Horiba-Jobin Yvon iHR320) fitted with a thermoelectrically cooled charge-coupled device camera. The experiments were performed at different temperatures in the 20–300-K range using an ultralow vibration closed-cycle refrigerator.

Transient reflectivity measurements to study carrier dynamics were performed in the degenerate pump-probe geometry using ≈100-fs-long pulses at a repetition rate of 80 MHz from a mode-locked Ti: sapphire laser. The pump beam was chopped at a frequency of 50 kHz using a photoelastic modulator. The spot diameter of the pump beam was ≈25 μm, and the average pump fluence used for all the measurements was ≈80 $\mu J/cm^2$. The intensity change in the reflected probe was recorded using a photodiode and a lock-in-amplifier. The pump wavelength is tuned from 750 to 810 nm for near- to below-resonant excitation.

## III. RESULTS AND DISCUSSION

The PL spectra of two exfoliated bilayer flakes, D1 and P1, obtained at room temperature and 20 K, are shown in Figs. 1(a) and 1(b), respectively. At room temperature, the PL emission from flake P1 (D1) has a dominant peak near ≈1.57 eV (1.52 eV). The initial characterization of the exfoliated $Mo_{0.6}W_{0.4}Se_2$ flakes was performed using room temperature PL measurements, as shown in Supplemental Material Fig. S5(a) [16]. The room-temperature PL spectra of the flakes resulted in categorizing the samples into two groups in terms of their PL peak energy and full width at half maximum (FWHM), as shown in Supplemental Material Fig. S5(b) [16]. For the first group, the position of the dominant PL peak is $1.57 \pm 0.01$ eV, and FWHM is approximately $51 \pm 6$ meV, which is lower compared to the second group, and P1 belongs to this first group. In the first group, the

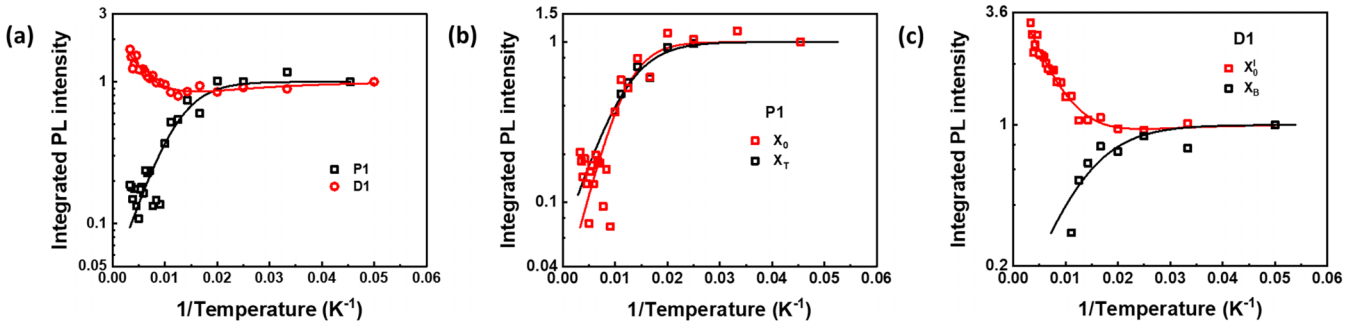


FIG. 2. (a) The total integrated PL intensity (normalized to the low-temperature intensity) versus the reciprocal of temperature for the two samples. The integrated PL intensity (normalized to the low-temperature intensity) of (b) $X_0$ and $X_T$ in sample P1 and (c) $X_B$ and $X_0'$ in sample D1 versus the reciprocal of temperature. The solid lines are fits to the data as discussed in the main text.

PL peak observed at room temperature can be decomposed into two peaks, as shown in Fig. 1(a)—the higher energy peak, which matches the direct transition, is the dominant one, while the second peak matches the indirect transition. The energy of the dominant PL peak observed in the first group matches well with the direct gap recombination in few-layered $Mo_{0.6}W_{0.4}Se_2$ [10], indicating that direct gap recombination dominates in the first group of samples. The FWHM of the second group is approximately $90 \pm 11$ meV with a peak position of $1.52 \pm 0.01$ eV, and D1 belongs to this second group. The PL peak in the second group matches well with the indirect gap recombination reported earlier in a few layered $Mo_{0.6}W_{0.4}Se_2$ [10]. The differences in the thicknesses of the flakes would introduce shifts up to about 12 meV in the PL peak position between the thinnest (monolayer) and the thickest (six-layered) flake [21,22]. However, in this study, we ignore the differences in the PL peak position between the different flakes and focus more on the temperature dependence of the PL intensity observed in different flakes.

The low temperature (20 K) PL spectra of P1 indicate the presence of the neutral exciton $X_0$ and a trion $X_T$ at ≈30 meV lower than $X_0$. The energy of $X_0$ and $X_T$ in P1 at low temperatures agrees well with earlier reports [23]. In the case of D1 at low temperature, the indirect exciton emission $X_0'$ at ≈1.6 eV and another peak at ≈109 meV lower than $X_0'$, which we assign to an exciton bound to a charged defect $X_B$, is observed. Since the material is an alloy, the sources of defects in mechanically exfoliated flakes could be vacancies or defects [24–28]. As reported earlier, $X_B$ consists of one valence band hole and one conduction band electron, forming an exciton that is bound to a negatively charged defect lying ≈109 meV below the CBM [14]. The trion peak is absent in D1 and the other flakes in the second group, possibly because of the high degree of compensation due to the defects [14]. The most common defects in TMDCs are chalcogen vacancies, which eventually create a midgap state closer to the conduction band [20,22–24]. The band structure calculations using DFT confirm the presence of midgap states due to chalcogen vacancies, as shown in Supplemental Material Fig. S6 [16]. The defect-bound exciton peak $X_B$ emerges at low temperatures when such defects trap neutral excitons. We focus on the dynamics of carriers trapped at these defects using temperature-dependent PL and ultrafast pump-probe measurements.

Figures 1(c) and 1(d) show the temperature-dependent PL spectra of samples P1 and D1, respectively. The energy of $X_0$ (and $X_T$) in sample P1 and $X_0'$ in sample D1 monotonously decreases with increasing temperature, and no abrupt jump in PL peak energies with temperature is observed. We do not observe any indication of temperature-induced transition from direct to indirect band-gap recombination [29]. The intensity of $X_0$ (and $X_T$) in sample P1 decreases with increasing temperature, while the intensity of $X_0'$ in sample D1 increases with increasing temperature. The $X_B$ intensity decreases with increasing temperature and disappears above ≈100 K.

The temperature dependence of the overall PL intensity, integrated over the whole spectral region covering both the peaks in D1 and P1, is shown in Fig. 2(a). The temperature dependence of the overall PL intensity for two more samples, P2 (monolayer) and D2 (trilayer), is shown in Supplemental Material Fig. S7 [16]. P1 and P2 both belong to the first group, and the overall PL intensity decreases with an increase in temperature in both P1 and P2. However, there is an increase in the overall PL intensity with an increase in temperature, i.e., NTQ of the PL in samples D1 and D2, both of which belong to the second group. NTQ is observed in multilayered flakes belonging to the second group in which, at low temperatures, an exciton bound to a charged defect $X_B$ is observed.

In general, the PL intensity in Mo-based TMDCs such as $MoSe_2$ decreases with increasing temperature. In contrast, the intensity of PL from W-based TMDCs $WSe_2$ increases with an increase in temperature, resulting in a nonmonotonous PL intensity evolution with a temperature increase in the $Mo_xW_{1-x}Se_2$ alloy [12,23]. The temperature dependence of the PL intensity in the Mo-rich ternary alloy $Mo_xW_{1-x}Se_2$ is similar to that in $MoSe_2$, and sample P1 follows this trend [12]. However, the temperature dependence of the PL intensity of sample D1 is similar to $WSe_2$ and W-rich $Mo_xW_{1-x}Se_2$ alloys [30]. Hence, one possibility is that the bulk $Mo_xW_{1-x}Se_2$ crystal is nonuniform and has W-rich and Mo-rich regions. The $A_{1g}$ Raman mode of the $Mo_{1-x}W_xSe_2$ alloy is sensitive to the alloy composition and shows a distinct shift with a change in the Mo/W content. Since the area probed by the Raman and PL measurements are similar and equal to the spot size of the laser (≈3 μm diameter), Raman measurements are ideal for verifying the variation of composition between different flakes. However, as shown in

Supplemental Material Fig. S3 [16], the Raman measurements show no observable shift in the $A_{1g}$ mode. Hence, we can discount the possibility of spatial variation in the composition of the alloy, causing the differences in behavior between the two groups of flakes.

It has also been reported that the disorder potential in ternary alloys leads to a nonmonotonous temperature dependence of the PL intensity [23]. Such disorder potential causes the localization of electrons and holes with energy below the band edges and gives rise to the S-shaped temperature dependence of the PL peak energy [23]. However, the monotonous temperature dependence of PL intensity and the absence of the S-shaped temperature dependence of the PL peak energy, which is discussed later, allow us to discount the possibility of the extra disorder potential present in the ternary system causing the anomalous temperature dependence of the PL intensity in sample D1.

The temperature-dependent PL intensity data are fitted using the Shibata model [31],

$$\frac{I_T}{I_0} = \frac{1 + \alpha e^{-\Delta E_{l\to r}/k_B T}}{1 + \beta e^{-\Delta E_{r\to h}/k_B T}},$$

where $\Delta E_{l\to r}$ represents the activation energy for the thermal excitation of electrons to the radiative state from a lower energy state and $\Delta E_{r\to h}$ is the activation energy for the transition of the electrons in the radiative state to a higher energy state, usually a nonradiative state; $\alpha$ and $\beta$ are the corresponding proportionality constants, and $k_B$ is the Boltzmann constant. In the absence of thermal excitation of electrons from a lower energy state ($\alpha = 0$), the above equation becomes the well-known Arrhenius equation [32].

In semiconductors, as the temperature rises, nonradiative recombination becomes prevalent over radiative recombination, causing a decrease in the PL intensity with increasing temperature, and this behavior could be fit using the Arrhenius equation [32]. In fact, the temperature dependence of the PL intensity in sample P1, shown in Fig. 2(a), fits well with the Arrhenius equation and an activation energy $\Delta E_{r\to h} = 22 \pm 3$ meV is obtained, which matches well with other reports [33,34]. In sample P1, the reduction in PL intensity at higher temperatures is due to nonradiative recombination channels with an activation energy of ≈22 meV.

In the case of sample D1, the temperature dependence of the PL intensity fits well with the Shibata model, shown in Fig. 2(a), which suggests that two competing processes govern the temperature dependence of the PL intensity: thermal excitation of electrons to the radiative state from a lower energy state and the transition of electrons from the radiative state to a higher energy state. From the fitting, we obtain the energy scales of the thermal activation of electrons from the lower energy states, which results in the anomalous rise of the PL intensity as $\Delta E_{l\to r} = 22 \pm 5$ meV, and the ratio $\alpha/\beta \approx 5$ suggests that the thermal activation of electrons dominates over the transition to nonradiative recombination channels. The PL from flakes belonging to the first (second) group has a temperature dependence similar to that of P1 (D1), as shown in Supplemental Material Fig. S7 [16].

Analyzing the evolution of the PL intensity of the individual peaks in these samples allows us to understand the underlying mechanism responsible for the anomalous temperature dependence observed in sample D1. Hence, the PL spectra were deconvoluted with two Gaussian functions. The peak positions and linewidths of $X_0$ and $X_T$ in sample P1 obtained from the fitting of peaks are shown in Figs. S8(a) and S8(b) [16]. The $X_0$ energy decreases with increasing temperature and is fitted with O'Donnell's equation [35]. The linewidth of $X_0$ broadens with the rise in temperature and is fitted using Rudin's equation [36].

Similarly, the temperature dependence of the $X_0'$ energy and its linewidth in sample D1 fit well with O'Donnell's and Rudin's equations, respectively, as shown in Fig. S9 [16]. However, $X_B$ disappears above ≈100 K, showing a slight blueshift with increasing temperature. The parameters obtained from the fitting are tabulated in Supplemental Material Table S1 [16] and match well with the reported values [21,22].

In sample P1, the temperature dependence of the $X_0$ and $X_T$ intensities follows the Arrhenius equation, as shown in Fig. 2(b). However, in sample D1, the temperature dependence of the $X_B$ and $X_0'$ intensities presents two scenarios, as shown in Fig. 2(c). The $X_B$ intensity follows the Arrhenius equation [32], which shows that $X_B$ dissociates as temperature increases, which results in the quenching of the $X_B$ intensity with an increase in temperature. As mentioned earlier, $X_B$ consists of one valence band hole, one conduction band electron, and one electron bound to the defect state, as schematically shown in Fig. 3 [14]. The dissociation of $X_B$ results in a charged defect along with a neutral exciton [14]. Hence, the dissociation of $X_B$ would consequently cause an increase in the intensity of $X_0'$. The activation energy obtained from fitting the temperature-dependent $X_B$ PL intensity represents the dissociation energy of $X_B$, which results in a charged defect and a neutral exciton, $X_0'$. From fitting the temperature-dependent data for the $X_B$ intensity, we obtain the activation energy for dissociation of $X_B$ as $15 \pm 6$ meV, which is much smaller than its binding energy (≈109 meV).

Furthermore, the temperature dependence of $X_0'$ fits well with the Shibata model, and from the fitting, we obtain the activation energy for the thermal excitation of electrons to $X_0'$ from a lower energy state, $\Delta E_{l\to r} = 19 \pm 8$ meV, which agrees with the dissociation energy of $X_B$ estimated from fitting the temperature-dependent $X_B$ intensity. This agreement between the activation energy for the thermal excitation of electrons to $X_0'$ and the dissociation energy of $X_B$ confirms that as the temperature increases, $X_B$ dissociates into a neutral exciton and a charged defect [14], leading to an increase in the intensity of $X_0'$ and a decrease in the intensity of $X_B$.

The effect of defect-related relaxation pathways on the carrier dynamics could be further studied using pump-probe spectroscopy by varying the pump energy from near- to below-exciton resonance conditions. The pump pulse excites carriers into the conduction band, and the increase in carrier population results in Pauli blocking, which reduces the absorption of the probe beam, which can be seen as a transient increase in probe reflectivity at early times. Defects quickly trap and localize the carriers on a timescale of a few ps. Absorption of the probe by the defect-trapped carriers leads to a transient decrease in the probe reflectivity. Hence, pump-probe spectroscopy can provide valuable insights into the

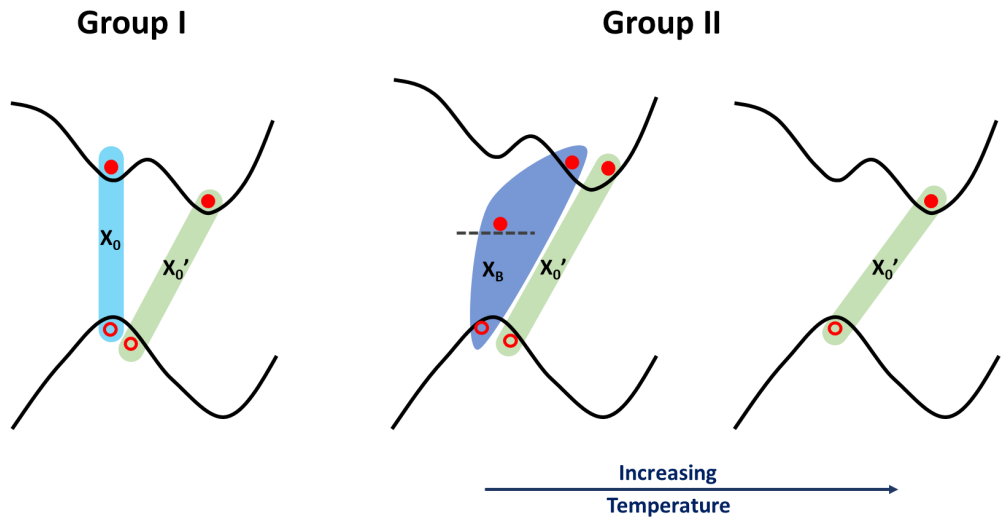


FIG. 3. Schematic band diagram and the optical transitions in the two groups of samples.

dynamics of carriers localized at defects. Figures 4(a) and 4(b) show the low temperature (≈7 K) transient reflectivity spectra of samples P1 and D1, respectively, obtained at different pump-probe excitation wavelengths. The pump-probe reflectivity shows multiexponential behavior, which implies more than one relaxation pathway. We modeled the experimental data using three independent exponential relaxation processes: (i) a fast relaxation process, which accounts for the initial cooling of the hot carriers; (ii) a slower relaxation process, which accounts for the recombination of carriers near the band edge; and (iii) a third process, which takes into account the relaxation of carriers trapped at the defects. $\tau_1$, $\tau_2$, and $\tau_3$ are the characteristic decay times associated with the three relaxation processes, and $A_1$, $A_2$, and $A_3$ are the corresponding amplitudes.

For sample P1, at a pump-probe wavelength of 750 nm (1.653 eV), where the pump energy is higher than the $X_0$ energy, the transient reflectivity shows a fast exponential decay ($\tau_1 \approx 230$ fs) followed by a slower decay component ($\tau_2 \approx 6$ ps). The pink- and green-shaded regions indicate these two processes in Fig. 4(a). Similar behavior is observed at other pump-probe energies, $E \gtrsim X_0 - 2\text{LA}$, where 2LA refers to twice the energy of the longitudinal acoustic (LA) phonons in the alloy. The fast decay component is due to the initial thermalization of the hot carriers, and the slow component is due to the final recombination of the carriers near the band edge [37]. At pump-probe energies, $E \lesssim X_0 - 2\text{LA}$, a transient decrease in the reflectivity is observed due to the intraband absorption [38].

For sample D1, at a pump-probe wavelength of 770 nm (1.61 eV), where the pump energy is higher than the $X_0'$ energy, the overall transient reflectivity signal decays much faster than what was observed in sample P1, and the decay could not be resolved into two components. The transient reflectivity was fitted with a single exponential decay function [shown by the green shaded region in Fig. 4(b)], and we obtained a decay time, $\tau_2 \approx 1$ ps. The defect state in the band gap efficiently captures photogenerated carriers, leading to a reduction in the exciton population and recombination time [39]. Similar to P1, at pump-probe energies, $E \lesssim X_0' - 2\text{LA}$, a transient reflectivity signal due to intraband absorption is observed in D1. However, at pump-probe energies, $E \lesssim X_0'$ an additional decay process with a relatively slower rise time ($\tau_r \approx 3$ ps) and a decay time $\tau_3 \approx 6$ ps is observed, which is indicated by the cyan-shaded region in Fig. 4(b) and can also be clearly observed in the 2D contour plot shown in Supplemental Material Fig. S10 [16]. From the defect-induced absorption, we can understand that the defects capture the photoinduced carriers on a timescale of ≈3 ps, and recombination at the defects occurs on a timescale of ≈6 ps.

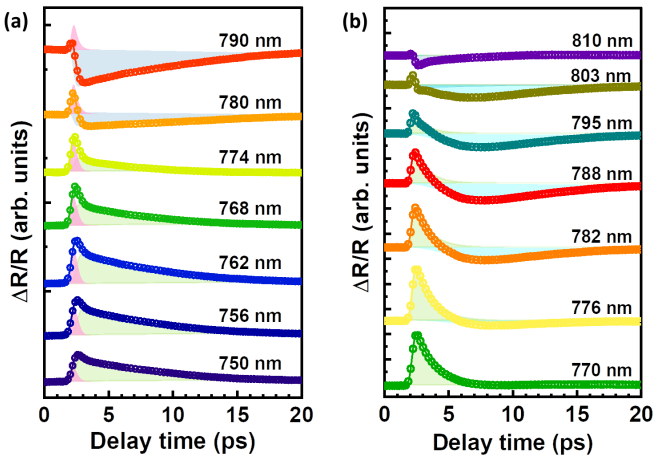


FIG. 4. Transient reflectivity at different pump wavelengths for the $Mo_{0.6}W_{0.4}Se_2$ samples (a) P1 and (b) D1 at ≈7 K. The symbols indicate the experimental data, and the solid lines are least-square fits to the data as described in the main text. The shaded regions indicate the different relaxation processes.

## IV. CONCLUSIONS

In summary, we studied the anomalous behavior of PL observed in mechanically exfoliated $Mo_xW_{1-x}Se_2$ flakes, bringing forth a systematic means to understand the role of defects in TMDC alloys. Using room temperature PL characterization, the exfoliated flakes were segregated into

two distinct groups. Compared to the flakes with narrower PL linewidths, which indicated a lower density of defects, flakes that showed broader PL linewidths showed a lower energy peak due to defect-bound excitons. The defective multilayered flakes showed negative thermal quenching of PL, and we showed that this is due to the dissociation of defect-bound excitons upon temperature increase, which leads to the enhancement of the neutral exciton intensity. Pump-probe studies showed faster recombination time in the flakes with defects, which is in agreement with the linewidth broadening. The carriers trapped at the defects cause a transient absorption of the probe in the flakes with defects, and from these measurements, we deduce that the carriers are captured at the traps on a timescale of ≈3 ps. Future studies using high-resolution microscopic techniques can provide further information about the microscopic details of the defects and their spatial distribution.

## ACKNOWLEDGMENTS

R.N.K. acknowledges funding support by the Science and Engineering Research Board, Department of Science and Technology, India, through Research Grants No. CRG/2019/004865 and No. IPA/2020/000021. The support for computing time at the IISER Thiruvananthapuram HPC cluster "Padmanabha" is also kindly acknowledged.

N.B. and P.K.B. exfoliated and characterized the flakes. N.B. performed the measurements, analyzed the data, and wrote the initial draft of the manuscript. J.N.S. performed the DFT calculations. R.N.K. supervised measurements and data analysis and prepared the final manuscript with input from all coauthors.

The authors declare that they have no known competing financial interests or personal relationships that could have appeared to influence the work reported in this paper.

[1] Y. Liu, K. Dini, Q. Tan, T. Liew, K. S. Novoselov, and W. Gao, Electrically controllable router of interlayer excitons, Sci. Adv. **6**, eaba1830 (2020).

[2] G. Scuri, T. I. Andersen, Y. Zhou, D. S. Wild, J. Sung, R. J. Gelly, D. Bérubé, H. Heo, L. Shao, A. Y. Joe, A. M. Mier Valdivia, T. Taniguchi, K. Watanabe, M. Lončar, P. Kim, M. D. Lukin, and H. Park, Electrically tunable valley dynamics in twisted $WSe_2/WSe_2$ bilayers, Phys. Rev. Lett. **124**, 217403 (2020).

[3] J. Yin, H. Wang, H. Peng, Z. Tan, L. Liao, L. Lin, X. Sun, A. L. Koh, Y. Chen, H. Peng, and Z. Liu, Selectively enhanced photocurrent generation in twisted bilayer graphene with Van Hove singularity, Nat. Commun. **7**, 10699 (2016).

[4] K. F. Mak and J. Shan, Photonics and optoelectronics of 2D semiconductor transition metal dichalcogenides, Nat. Photon. **10**, 216 (2016).

[5] W. Yao, D. Xiao, and Q. Niu, Valley-dependent optoelectronics from inversion symmetry breaking, Phys. Rev. B **77**, 235406 (2008).

[6] J. Yao, Z. Zheng, and G. Yang, Promoting the performance of layered-material photodetectors by alloy engineering, ACS Appl. Mater. Interfaces **8**, 12915 (2016).

[7] L. Ju, M. Bie, X. Tang, J. Shang, and L. Kou, Janus WSSe Monolayer: An excellent photocatalyst for overall water splitting, ACS Appl. Mater. Interfaces **12**, 29335 (2020).

[8] J. Yao and G. Yang, 2D group 6 transition metal dichalcogenides toward wearable electronics and optoelectronics, J. Appl. Phys. **127**, 30902 (2020).

[9] S. Masanta, C. Nayak, S. Maitra, S. Rudra, D. Chowdhury, S. Raha, M. Pradhan, B. Satpati, P. Pal, and A. Singha, Engineering multifunctionality in $MoSe_2$ nanostructures via strategic Mn doping for electrochemical energy storage and photosensing, ACS Appl. Nano Mater. **6**, 5479 (2023).

[10] M. Zhang, J. Wu, Y. Zhu, D. O. Dumcenco, J. Hong, N. Mao, S. Deng, Y. Chen, Y. Yang, C. Jin, S. H. Chaki, Y. Huang, J. Zhang, and L. Xie, Two-dimensional molybdenum tungsten diselenide alloys: Photoluminescence, Raman scattering, and electrical transport, ACS Nano **8**, 7130 (2014).

[11] L. M. Xie, Two-dimensional transition metal dichalcogenide alloys: preparation, characterization and applications, Nanoscale **7**, 18392 (2015).

[12] Y. Liu, K. Tom, X. Zhang, S. Lou, Y. Liu, and J. Yao, Alloying effect on bright–dark exciton states in ternary monolayer $Mo_xW_{1-x}Se_2$, New J. Phys. **19**, 073018 (2017).

[13] H. P. Komsa and A. V. Krasheninnikov, Two-dimensional transition metal dichalcogenide Alloys: Stability and electronic properties, J. Phys. Chem. Lett. **3**, 3652 (2012).

[14] V. Carozo, Y. Wang, K. Fujisawa, B. R. Carvalho, A. Mccreary, S. Feng, Z. Lin, C. Zhou, N. Perea-Lopez, A. L. Elias, B. Kabius, V. H. Crespi, and M. Terrones, Optical identification of sulfur vacancies: Bound excitons at the edges of monolayer tungsten disulfide, Sci. Adv. **3**, e1602813 (2017).

[15] H. Han, A. Lu, L. Lu, J. Huang, H. Li, C. Hsu, Y. Lin, M. Chiu, K. Suenaga, C. Chu, H. Kuo, W. Chang, L. Li, and Y. Shi, Photoluminescence enhancement and structure repairing of monolayer $MoSe_2$ by hydrohalic acid treatment, ACS Nano **10**, 1454 (2016).

[16] See Supplemental Material at http://link.aps.org/supplemental/10.1103/PhysRevMaterials.8.064005 for optical images, optical contrast images, AFM maps, height profiles, Raman spectra, additional photoluminescence data and wavelength-dependent pump-probe reflectivity data of exfoliated samples, XPS spectra, details of the optical contrast analysis, the temperature dependence of the PL peak energy and linewidth, band structure calculations, and computational details, which includes Ref. [18].

[17] M. M. Benameur, B. Radisavljevic, J. S. Héron, S. Sahoo, H. Berger, and A. Kis, Visibility of dichalcogenide nanolayers, Nanotechnology **22**, 125706 (2011).

[18] A. Bera, B. Kundu, U. K. Ghorai, and A. J. Pal, Alloyed transition-metal dichalcogenides ($Mo_{1-x}W_xSe_2$) through a hydrothermal synthesis route: Probing layer-number-dependent band energies and band-gap bowing via scanning tunneling spectroscopy, Phys. Rev. Mater. **7**, 014005 (2023).

[19] K. Chen, R. Ghosh, X. Meng, A. Roy, J. Kim, F. He, S. C. Mason, X. Xu, J. Lin, D. Akinwande, S. K. Banerjee, and Y.

Wang, Experimental evidence of exciton capture by mid-gap defects in CVD grown monolayer $MoSe_2$, npj 2D Mater. Appl. **1**, 15 (2017).

[20] B. Xia, D. Gao, P. Liu, Y. Liu, S. Shi, and K. Tao, Zigzag-Edge related ferromagnetism in $MoSe_2$ nanoflakes, Phys. Chem. Chem. Phys. **17**, 32505 (2015).

[21] A. Arora, K. Nogajewski, M. Molas, M. Koperski, and M. Potemski, Exciton band structure in layered $MoSe_2$: from a monolayer to the bulk limit, Nanoscale **7**, 20769 (2015).

[22] A. Arora, M. Koperski, K. Nogajewski, J. Marcus, C. Faugeras, and M. Potemski, Excitonic resonances in thin films of $WSe_2$: from monolayer to bulk material, Nanoscale **7**, 10421 (2015).

[23] H. Masenda, L. M. Schneider, M. Adel Aly, S. J. Machchhar, A. Usman, K. Meerholz, F. Gebhard, S. D. Baranovskii, and M. Koch, Energy scaling of compositional disorder in ternary transition-metal dichalcogenide monolayers, Adv. Electron. Mater. **7**, 2100196 (2021).

[24] N. Saigal and S. Ghosh, Evidence for two distinct defect related luminescence features in monolayer $MoS_2$, Appl. Phys. Lett. **109**, 122105 (2016).

[25] Z. Hu, Z. Wu, C. Han, J. He, Z. Ni, and W. Chen, Two-dimensional transition metal dichalcogenides: interface and defect engineering, Chem. Soc. Rev. **47**, 3100 (2018).

[26] S. V. Sivaram, A. T. Hanbicki, M. R. Rosenberger, G. G. Jernigan, H. Chuang, K. M. McCreary, and B. T. Jonker, Spatially selective enhancement of photoluminescence in $MoS_2$ by exciton-mediated adsorption and defect passivation, ACS Appl. Mater. Interfaces **11**, 16147 (2019).

[27] K. Greben, S. Arora, M. G. Harats, and K. I. Bolotin, Intrinsic and extrinsic defect-related excitons in TMDCs, Nano Lett. **20**, 2544 (2020).

[28] S. Tongay, J. Suh, C. Ataca, W. Fan, A. Luce, J. S. Kang, J. Liu, C. Ko, R. Raghunathanan, J. Zhou, F. Ogletree, J. Li, J. C. Grossman, and J. Wu, Defects activated photoluminescence in Two-dimensional semiconductors: interplay between bound, charged and free excitons, Sci. Rep. **3**, 2657 (2013).

[29] W. Zhao, R. M. Ribeiro, M. Toh, A. Carvalho, C. Kloc, A. H. Castro Neto, and G. Eda, Origin of indirect optical transitions in few-layer $MoS_2$, $WS_2$, and $WSe_2$, Nano Lett. **13**, 5627 (2013).

[30] X.-X. Zhang, Y. You, S. Y. F. Zhao, and T. F. Heinz, Experimental evidence for dark excitons in monolayer $WSe_2$, Phys. Rev. Lett. **115**, 257403 (2015).

[31] H. Shibata, Negative thermal quenching curves in photoluminescence of solids, Jpn. J. Appl. Phys. **37**, 550 (1998).

[32] G. Bacher, H. Schweizer, J. Kovac, A. Forchel, H. Nickel, W. Schlapp, and R. Lösch, Influence of barrier height on carrier dynamics in strained InxGa1-XAs/GaAs quantum wells, Phys. Rev. B **43**, 9312 (1991).

[33] X. Li, A. A. Puretzky, X. Sang, Santosh KC, M. Tian, F. Ceballos, M. Mahjouri-Samani, K. Wang, R. R. Unocic, H. Zhao, G. Duscher, V. R. Cooper, C. M. Rouleau, D. B. Geohegan, and K. Xiao, Suppression of defects and deep levels using isoelectronic tungsten substitution in monolayer $MoSe_2$, Adv. Funct. Mater. **27**, 1603850 (2017).

[34] J. S. Ross, S. Wu, H. Yu, N. J. Ghimire, A. M. Jones, G. Aivazian, J. Yan, D. G. Mandrus, D. Xiao, W. Yao, and X. Xu, Electrical control of neutral and charged excitons in a monolayer semiconductor, Nat. Commun. **4**, 1474 (2013).

[35] K. P. O'Donnell and X. Chen, Temperature dependence of semiconductor band gaps, Appl. Phys. Lett. **58**, 2924 (1991).

[36] S. Rudin, T. L. Reinecke, and B. Segall, Temperature-dependent exciton linewidths in semiconductors, Phys. Rev. B **42**, 11218 (1990).

[37] K. Chen, A. Roy, A. Rai, A. Valsaraj, X. Meng, F. He, X. Xu, L. F. Register, S. Banerjee, and Y. Wang, Carrier trapping by oxygen impurities in molybdenum diselenide, ACS Appl. Mater. Interfaces **10**, 1125 (2018).

[38] T. Gong, W. L. Nighan, and P. M. Fauchet, Hot-carrier Coulomb effects in GaAs investigated by femtosecond spectroscopy around the band edge, Appl. Phys. Lett. **57**, 2713 (1990).

[39] S. Zhang, L. Xu, P. Hu, K. Maaz, J. Zeng, P. Zhai, Z. Li, L. Liu, and J. Liu, Excitonic performance and ultrafast dynamics in defective $WSe_2$, Appl. Phys. Lett. **121**, 83102 (2022).